nature nanotechnology

Article

https://doi.org/10.1038/s41565-024-01658-6

# Phase-separated porous nanocomposite with ultralow percolation threshold for wireless bioelectronics

Received: 9 October 2023

Accepted: 25 March 2024

Published online: 29 April 2024

Check for updates

Yadong Xu[1,2,8], Zhilu Ye[3,8], Ganggang Zhao[4,8], Qihui Fei[1], Zehua Chen[1], Jiahong Li[2], Minye Yang[3], Yichong Ren[3], Benton Berigan[1], Yun Ling[4], Xiaoyan Qian[1], Lin Shi[1], Ilker Ozden[1], Jingwei Xie[5], Wei Gao[2] ✉, Pai-Yen Chen[3] ✉ & Zheng Yan[1,4,6,7] ✉

Realizing the full potential of stretchable bioelectronics in wearables, biomedical implants and soft robotics necessitates conductive elastic composites that are intrinsically soft, highly conductive and strain resilient. However, existing composites usually compromise electrical durability and performance due to disrupted conductive paths under strain and rely heavily on a high content of conductive filler. Here we present an in situ phase-separation method that facilitates microscale silver nanowire assembly and creates self-organized percolation networks on pore surfaces. The resultant nanocomposites are highly conductive, strain insensitive and fatigue tolerant, while minimizing filler usage. Their resilience is rooted in multiscale porous polymer matrices that dissipate stress and rigid conductive fillers adapting to strain-induced geometry changes. Notably, the presence of porous microstructures reduces the percolation threshold ($V_c$ = 0.00062) by 48-fold and suppresses electrical degradation even under strains exceeding 600%. Theoretical calculations yield results that are quantitatively consistent with experimental findings. By pairing these nanocomposites with near-field communication technologies, we have demonstrated stretchable wireless power and data transmission solutions that are ideal for both skin-interfaced and implanted bioelectronics. The systems enable battery-free wireless powering and sensing of a range of sweat biomarkers—with less than 10% performance variation even at 50% strain. Ultimately, our strategy offers expansive material options for diverse applications.

Soft elastic conductive composite materials that exhibit high electrical conductivity[1,2], strain-insensitive performance[3–5] and skin-like mechanical compliance[6–9] are essential for next-generation soft robotics, and for skin-mounted and implanted devices[10,11]. They are pivotal in biomedical diagnostics, electronic skins and human–machine interfaces[12–15]. System-level bioelectronic devices, composed of soft sensors and rigid electronic components[10,16], demand breathable sensors and strain-resilient conductors that offer exceptional mechanical tolerance. Present enabling technologies utilize conductive fillers dispersed in elastomer matrices, spanning from nanoparticles,

A full list of affiliations appears at the end of the paper. ✉e-mail: weigao@caltech.edu; pychen@uic.edu; yanzheng@missouri.edu

nanowires/nanotubes, to nanosheets[12,13]. Although liquid-metal-based composites have been established to be viable solution, their susceptibility to leakage, necessity of high loadings, and inevitable interface corrosion of electronic components over prolonged exposure pose challenges[17,18].

Due to percolation theory, metal nanowires with high aspect ratios are preferred over other fillers to achieve highly conductive composites because they considerably reduce the percolation threshold[12]. Recent endeavours span from the fabrication of silver nanowire (Ag NW) nanocomposites with notable electrical conductivity to ultrathin nanomembranes with facile patternability[1,2]. Nonetheless, persistent challenges remain, including pronounced electromechanical coupling, rapid degradation in cyclic fatigue test, tedious ligand exchange processes and the necessity for substantial filler loadings (60–80% by weight). Minimizing filler usage is essential to achieve cost-effectiveness, reduce macroscopic stiffness and enhance stretchability. Additionally, macroscale stretching of nanocomposites generally results in diminished overlap of percolation pathways, thereby compromising their electrical performance. Strain-induced self-organization and rearrangement of the conductive fillers within the polymer represents a promising strategy[19–21], yet the synthesis and separation of fillers from the polymer at the microscale level are fundamentally challenging.

Porous elastomer conductors, characterized by high breathability, ultrasoftness and large surface area, can find broad applications[9,22–24]. Various techniques, including hard-templating, freeze-drying, emulsion, breath figure methods and electrospinning, have been used to introduce porous structures[9,24,25]. Specifically, porous Ag NW elastomer composites with notable breathability have been achieved[26,27]. However, these methods often yield materials with notable electrical-mechanical coupling. In addition, phase separation has gained considerable attention for creating interconnected and tunable porous polymer structures in a simple, cost-effective and template-free manner[28,29]. Representative applications include thermal management, sensing, catalysis, energy storage and water purification[23,28,30]. Furthermore, phase separation has been applied to produce porous conductors by embedding conductive fillers within polymer matrices. However, these materials usually lack strain-insensitive properties[23,31].

Here we report a one-step, in situ phase separation of Ag NWs from porous polyurethane (PU) matrices (Fig. 1a). This process facilitates microscale assembly of Ag NWs, forming self-organized percolation networks on pore surfaces. Consequently, we achieve an electrically conductive phase-separated porous Ag NW nanocomposite (PSPN) with extremely low percolation threshold and strain-insensitive electrical properties. The latter arise from the synergy of energy-dissipative porous PU microstructures and adaptable Ag NW conductive pathways, maintaining effective electron transport even under notable macroscopic strain (Fig. 1b,c). We demonstrate simultaneous accomplishment of electrical-mechanical decoupling, ultralow percolation thresholds and remarkable electrical conductivity despite the low Ag NW volume fractions. This strategy also eliminates the ligand-exchange process typically required for Ag NW-based composites. Leveraging these unique attributes, we pair our PSPN with near-field communication (NFC)-based technologies to achieve wireless power delivery and data transmission for skin-interfaced and implantable bioelectronic devices.

## Phase separation and theoretical prediction

The fabrication of PSPN begins with the preparation of a precursor solution containing polymer solution (PU in tetrahydrofuran (THF)) and conductive filler solution (Ag NWs in ethanol). During the subsequent drop-casting process, phase separation initiates due to the evaporation of the volatile solvent (THF) and non-solvent (ethanol). This results in the separation of the PU-rich and PU-poor phases. Ag NWs with amphiphilic ligands (that is, polyvinyl pyrrolidone) reside in the PU-poor phase due to its immiscibility with PU solution. The liquid–liquid demixing process generates co-continuous phases in three dimensions, completed by coarsening that creates continuous porous structures within the PU matrices. Figure 1a presents a two-dimensional (2D) cross-sectional view of the phase-separation process, whereas Supplementary Fig. 1 provides a complementary 3D schematic of the PSPN. This process can be elucidated by examining the trajectory of the compositional path of the nanocomposite solution within the phase diagram (Fig. 1d)[28,29,32,33]. The pore sizes are tunable by changing the non-solvent content (Supplementary Fig. 2). Throughout this process, Ag NWs initially self-organize closely on the pore surfaces, gradually forming strain-adaptive percolation networks characterized by an increasing number of nanowires. As illustrated in Supplementary Fig. 3, the natural evaporation of THF and ethanol is essential for the formation of porous nanocomposites. The microscopic-level self-assembly of Ag NWs, guided by the presence of microsized pores, is driven by minimizing the free energy to stabilize the system (that is, the Pickering effect)[34].

Conductive nanocomposites are generally made by uniformly dispersing conductive filler materials within soft elastomer matrices, where these nanomaterials establish conductive percolation networks (that is, multiple continuous electron transport paths) once a critical density is reached[12]. For example, strain-induced rupture of Ag NW percolation networks typically occurs upon macroscopic stretching[19] (Fig. 1c). In the presence of an energy-dissipative porous microstructure, on the contrary, soft polymer matrices alter the deformation, accommodate the mechanical strain and dissipate local stress, whereas strain-adaptive Ag NW percolation pathways adapt to such structural change due to substantial mechanical mismatch and therefore preserve interconnected conductive networks (Fig. 1b). Numerical calculations of tunnelling resistance[35,36] among Ag NWs together with finite-element analysis (FEA) simulations provided a quantification of the electrical variations (Supplementary Note 1). As shown in Fig. 1e, PSPN exhibits a marginal increase in electrical resistance across a broad range of uniaxial strains, whereas conventional non-porous nanocomposite experiences a rapid resistance increase, followed by an abrupt electrical failure due to the development and propagation of microscopic cracks within Ag NW networks. This noticeable disparity signifies a considerably improved stretchability in the porous nanocomposites, showcasing exceptional electrical-mechanical decoupling. Furthermore, we apply a theoretical calculation based on 3D percolation theory[37] to correlate the percolation threshold $V_c$ (that is, the minimum number

**Fig. 1 | Schematic and fabrication of strain-insensitive PSPN with ultralow percolation thresholds. a**, Schematic illustration of a cross-sectional view of the phase-separation process. **b**,**c**, Schematic of porous (**b**) and non-porous (**c**) Ag NW nanocomposites in original (left) and stretched (right) states. **d**, Schematic illustration of the isothermal ternary phase diagram of polymer, solvent and non-solvent (that is, PU, THF and ethanol). The composition path in the phase diagram illustrates the trajectory of the multicomponent system as it transitions across various phases due to the evaporation of the solvent and non-solvent. The initial solution represents the composition of the original casting solution at the outset of this process. In brief, the initial casting solution, composed of solvent, non-solvent and polymer, forms a homogeneous solution. Upon the evaporation of solvent and non-solvent, the trajectory of the composition path crosses the binodal and spinodal, entering the unstable region where liquid–liquid demixing occurs (two phases). The spinodal decomposition reduces the free energy of the system through diffusion and fluid flow or convection. Such mass transfer leads to the formation of bicontinuous porous structures. **e**, Numerical calculation of the evolution of electrical resistance as a function of applied strain on non-porous (black) and porous (red) nanocomposites. Dashed lines depict the exponentially fitted data. **f**, Theoretical calculation of percolation thresholds for non-porous (purple) and porous (red) Ag NW nanocomposites, demonstrating their dependency on pore size. **g**, Optical photograph of a 500% stretched, free-standing PSPN. Scale bar, 1 cm.

https://doi.org/10.1038/s41565-024-01658-6

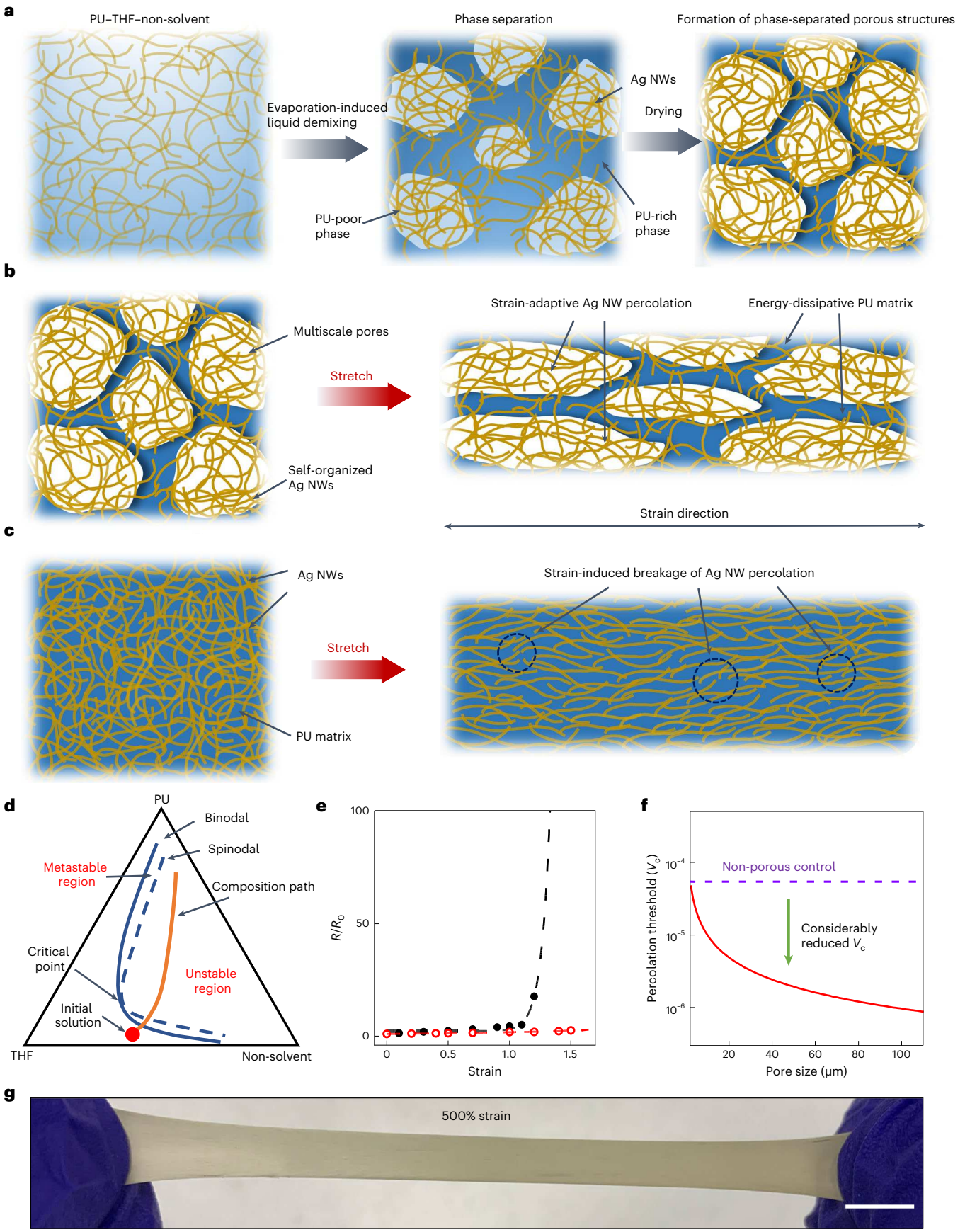

of conductive fillers required to create conductive pathways) with the pore size $D_p$ of the polymer matrix (Supplementary Note 2):

$$V_c = \frac{1.4093\pi d^2}{Vl} f(D_p)$$

where $d$ and $l$ are the diameter and length of the nanowire, $V$ is the volume of the nanocomposite and $f(D_p)$ is the surface area of the porous microstructure as a function of pore size $D_p$. The presence of microscale porous structure results in a percolation threshold orders of magnitude lower than that observed in non-porous nanocomposites (Fig. 1f). Furthermore, the electrical conductivity also depends on the $D_p$ of the porous composites (Supplementary Note 3). Despite the low volume fractions of conductive fillers, the PSPN obtained with high electrical conductivity and stretchability consistently aligns with the results of these numerical examinations (Fig. 1g).

## Strain-resilient property and ultralow percolation threshold

We experimentally demonstrated the self-assembly of Ag NWs at the interface of a continuous 'solid–gas' phase as the concentration of Ag NWs increases (Fig. 2a). Such selective distribution substantially reduces the volume fraction of conductive fillers required for continuous electron transport, in contrast to conventional non-porous nanocomposite where filler materials are nearly homogeneously distributed. To understand the impact of porous microstructures, we quantitatively evaluated the electrical conductivity of PSPN and non-porous nanocomposite as a function of Ag NW volume fractions. The data in Fig. 2b were fitted using 3D percolation theory (Supplementary Note 4)[38]. We observed a notable reduction in percolation threshold ($V_c$) from 0.02971 to 0.00131 (a factor of ~22) with the existence of porous microstructures (mean pore size, ~6.4 µm). Based on our theoretical analysis presented in Fig. 1f, we empirically validated that the percolation threshold is influenced by pore size. We note that the addition of 1-butanol as co-non-solvent allows broader control over pore sizes compared with the porous nanocomposite made with ethanol, when varying the volumetric ratios between PU solution and Ag NW solution (Supplementary Figs. 2 and 4). Furthermore, there was a 48-fold decrease in the threshold ($V_c$ = 0.00062) with an increase in pore size to ~16.8 µm (Supplementary Fig. 5) compared with non-porous nanocomposites. This is among the lowest thresholds ever reported (Supplementary Tables 1 and 2). The electrical conductivity differs depending on Ag NW volume fractions, reaching an optimum value of ~642,000 S m$^{-1}$ ($V_{Ag\ NWs} \approx 0.007$) after cold welding with saturated sodium chloride or sodium borohydride solution.

The PSPN comprises randomly distributed Ag NWs confined within the porous polymer matrices. The Ag NWs establish conductive percolation networks, effectively bridging interconnected pores across multiple scales (Fig. 2c, left). The notable mechanical mismatch in Young's modulus between soft PU elastomer (~16 MPa) and rigid Ag NWs (~83 GPa) generates anisotropic regions with different elasticity. Upon stretching, local stress dissipation is achieved through autonomous structural alternation of the soft PU elastomer, while the strain-adaptive Ag NWs retain the original percolation networks with minimally altered orientation (Fig. 2c, middle and right). As a result, this enables delayed electrical failure (>600%), and notably stabilized electrical resistance under large uniaxial ($R/R_0$ = 1.5 at 100% and 20.2 at 500%; Fig. 2d and Supplementary Fig. 6) and biaxial strains, and bending (Supplementary Fig. 7). In contrast, electrical failure in non-porous nanocomposites occurs at an early stage (~100%), primarily because they lack energy-dissipative porous microstructures, resulting in the rupture of percolation pathways (Supplementary Fig. 8). Our strategy's superiority is further demonstrated by recording electrocardiogram signals using electrical wiring made from our PSPN and conventional Ag NWs (Supplementary Fig. 9 and Supplementary Video 1).

In Fig. 2e and Supplementary Fig. 10, we compare the evolution of electrical resistance of PSPN with other representative materials. Remarkably, our porous conductor exhibits substantially smaller variations in resistance compared to a variety of porous and non-porous composites. Furthermore, our porous conductor exhibits outstanding durability and reliability, as evidenced by a slight resistance change ($R/R_0$ = 5.4) after cyclic stretching of 50% for 10,000 cycles, in evident contrast to that of the non-porous control ($R/R_0$ = 262; Fig. 2f). The susceptibility to fatigue-induced electrical performance degradation in the non-porous nanocomposite aligns with previous findings on silver flakes/nanoparticles, in which performance deteriorates abruptly with increased stretching cycles[4]. Such exceptionally durable performance of the porous nanocomposite can also be extended to larger strains (Supplementary Fig. 11). Moreover, we found that alcohol (for example, ethanol) treatment can facilitate the recovery of electrical resistance following stretching in our porous nanocomposite, whereas negligible effect was observed in the non-porous counterpart (Supplementary Fig. 12). This phenomenon arises from capillary forces generated during ethanol evaporation, which facilitates cold sintering of the inter-nanowire junctions of the Ag NWs[39]. We also demonstrate its resilience to multiple washing cycles (Supplementary Fig. 13) and various damage scenarios, including puncturing with a scalpel knife, impact loading from a hammer strike, twisting and bending (Fig. 2g and Supplementary Video 2). This outstanding performance can be attributed to the energy-dissipating porous PU microstructures, which dampen external mechanical impacts, and the robust interface formed by hydrogen bonding between Ag NWs and PU (Supplementary Fig. 14)[9]. Here, we utilized PSPN at a thickness of ~200 µm to fabricate wireless stretchable bioelectronics. Varying the thickness of PSPN by adjusting the casting solution per unit surface area shows a trivial impact on its electromechanical performance (Supplementary Fig. 15). Notably, our porous conductive nanocomposite also remains electrically stable over 60 days under ambient conditions, 3 h under ultraviolet/ozone ($UV/O_3$) treatment, and 30 min of wearing with heavy skin perspiration (Supplementary Fig. 16). In addition, we note that the electrical conductivity, modulus and electromechanical properties of the resulting porous nanocomposites are tunable by varying the volumetric ratios between the PU and Ag NW solutions (Supplementary Fig. 17) and the post-annealing temperature (Supplementary Fig. 18).

Furthermore, the multiscale interconnected cellular structure enables enhanced porosity and breathability to facilitate skin perspiration and improve long-term biocompatibility. We note a substantial increase in water vapour transmission rate (WVTR) from ~615 to ~4,424 g m$^{-2}$ day$^{-1}$ and a reduction in Young's modulus from ~9.1 to ~1.6 MPa in the presence of the porous structure (Fig. 2h). Given that the material's elastic modulus $E$ scales with its density $\rho$, $E/E_s \propto (\rho/\rho_s)^n$ (ref. 40), where the power ($n$) is associated with the porous material's nano/microstructures, we attribute the increased softness to the multiscale nano- and microstructures. This feature promotes a compliant interface with biological tissues[41]. Finally, we provide a comprehensive comparison of our PSPN with other state-of-the-art soft porous and non-porous conductors in terms of percolation threshold, strain insensitivity, stretchability, electrical conductivity and breathability. Detailed comparisons are provided in Fig. 2i[2,31,42–45], Supplementary Fig. 10 and Supplementary Tables 1 and 2. It is worth noting that high electrical stability under large strain is achieved by coating liquid metals on fibre mat surfaces[46]. However, this composite faces challenges such as performance degradation during skin rubbing and other limitations inherent in liquid-metal-based composites.

## Strain-insensitive wireless powering system

Wireless power delivery is emerging in the realm of wearable and soft electronics because it eliminates the use of batteries[47–49]. Here we fabricate stretchable spiral coils using our PSPN and implement these in a radiofrequency (RF) wireless power transfer (WPT) system.

https://doi.org/10.1038/s41565-024-01658-6

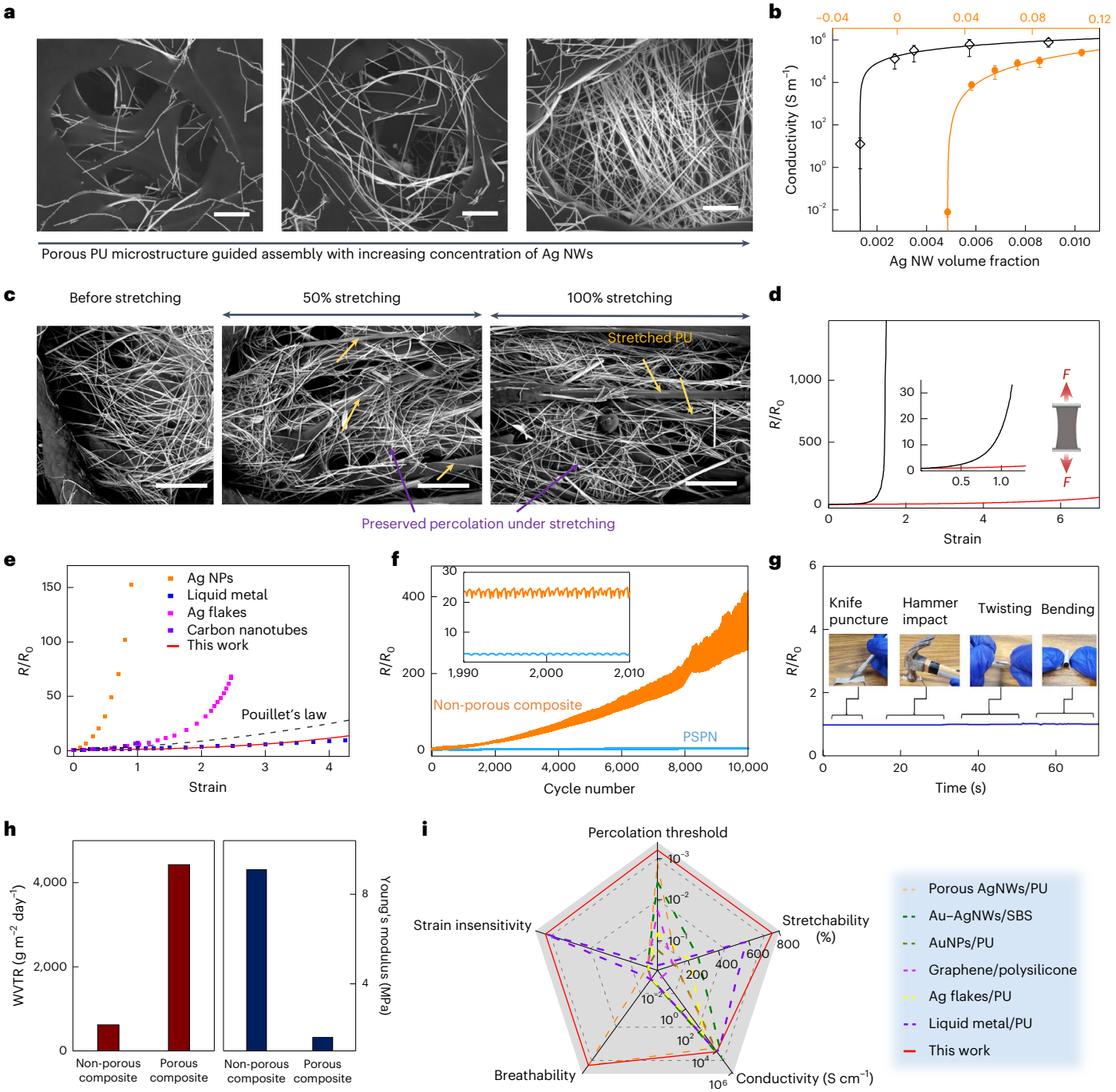


**Fig. 2 | Phase-separation, electrical and mechanical characterization.** **a**, SEM micrographs of PSPN with increased Ag NW concentrations. Scale bars, 2 µm. **b**, Electrical conductivities of non-porous composite (orange) and PSPN (black; pore size, ~6.4 µm) as a function of Ag NW volume fractions. Error bars represent the s.d. of the mean from six samples. Data are fitted using the 3D percolation theory. **c**, SEM images of PSPN before (left) and after stretching (middle, 50%; right, 100%). Scale bars, 5 µm. **d**, Relative resistance change ($R/R_0$) of non-porous nanocomposite (black) and PSPN (red) as a function of uniaxial strain. **e**, Comparison of electromechanical characteristics with other reported elastic conductors. Data were extracted from previous reports as summarized in Supplementary Fig. 10. **f**, Relative resistance changes of non-porous (orange) and porous (blue) nanocomposites subjected to cyclic stretching (50% maximum strain) for 10,000 cycles. Inset: magnified resistance variations over a 20-cycle period. **g**, Demonstration of PSPN resilience to punctures from a scalpel blade, hammer impact, twisting and bending. **h**, Water vapour transmission rate (WVTR; left) and Young's modulus (right) of non-porous nanocomposites and PSPN, illustrating the substantial increase in breathability and reduction in modulus with the presence of porous microstructures. **i**, Radar chart of the characteristics of this work compared with other soft conductive composites. Note that breathability and strain insensitivity are qualitative values. Detailed comparison can be found in Supplementary Tables 1 and 2. In short, our PSPN exhibits a distinctive combination of multiple desired features, such as ultralow percolation threshold, outstanding strain-insensitive electrical conductance, high stability and others, which represents a valuable addition to existing conductive composites for stretchable electronics. The non-porous composites in **d**,**f** were achieved by collapsing the porous microstructure of PSPN with THF vapour treatment (60 °C, overnight).

https://doi.org/10.1038/s41565-024-01658-6

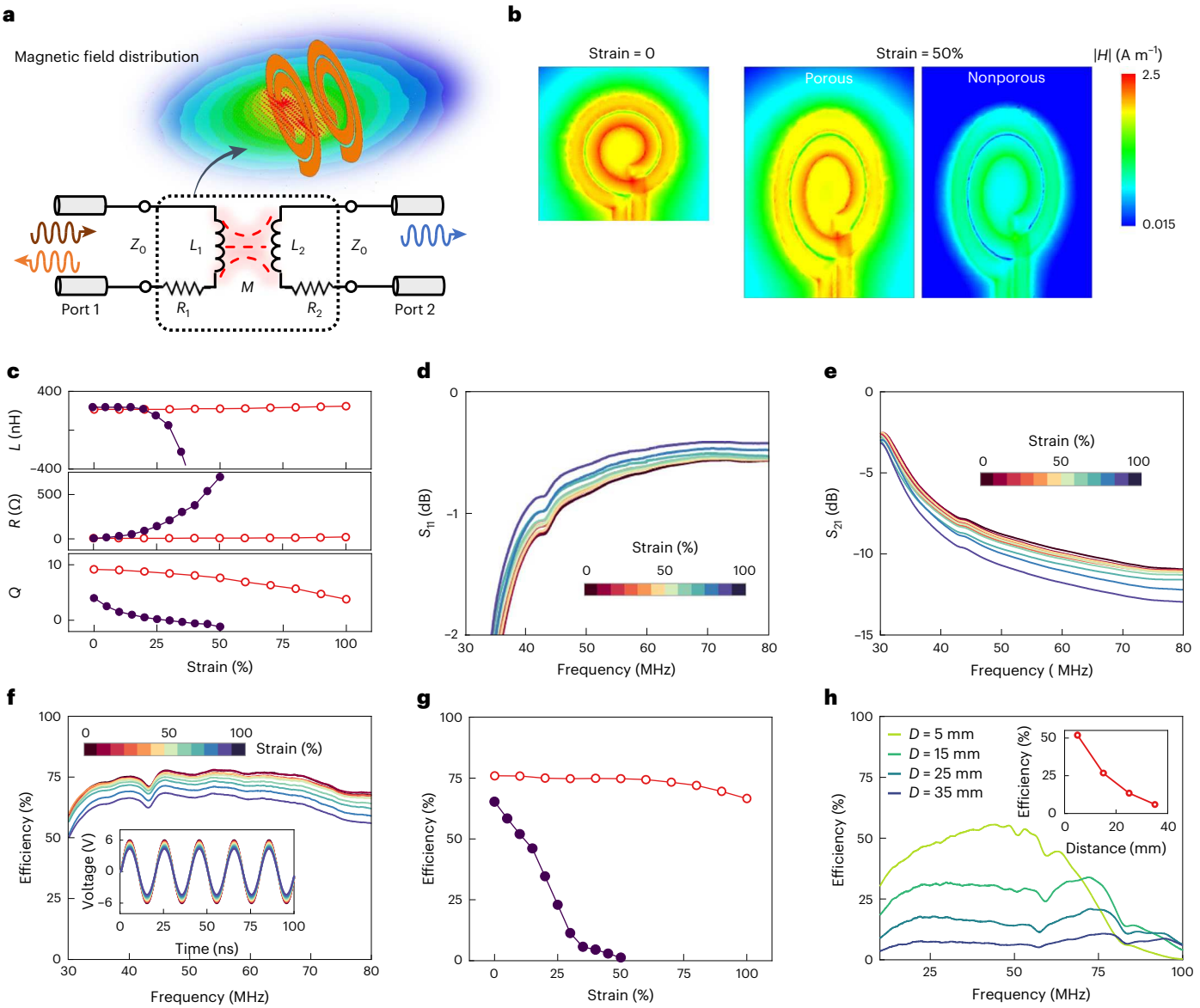


**Fig. 3 | Radiofrequency properties of the stretchable PSPN coils under tensile strain. a**, Two-port network model of the stretchable WPT system with the corresponding magnetic field distribution. **b**, Numerical simulations of magnetic field distributions of the porous and non-porous nanocomposites under 50% strain. **c**, Inductance $L$, resistance $R$ and quality factor $Q$ of PSPN (red) and non-porous nanocomposite (blue) at 50 MHz as functions of uniaxial tensile strain. **d**–**f**, Scattering parameters $S_{11}$ (**d**) and $S_{21}$ (**e**), and power transfer efficiency $\eta$ (**f**) of the two-port WPT system comprising a primary transmitter coil and a stretchable receiver coil made from PSPN under strain. Inset in **f**: theoretical calculations of induced voltage on the stretchable receiver coil at 50 MHz under strain. **g**, The evolutions of power transfer efficiency at 50 MHz of PSPN (red) and non-porous nanocomposite (blue) as a function of tensile strain. **h**, Power transfer efficiency between the primary transmitter and porous nanocomposite receiver coils at various vertical distances. Inset: extracted data at 50 MHz.

Figure 3a shows the two-port network model of the WPT system, and the magnetic field distribution of the transmitter and receiver coils under RF excitation. To evaluate the performance of the PSPN in wireless communication technology, we first theoretically examined the magnetic field distribution using Ansys Maxwell simulation (Fig. 3b). Despite comparable performances in the unstretched state, the porous coil remains largely unchanged, while the non-porous one experiences a substantial reduction in magnetic field at 50% strain. This is ascribed to the stable electrical resistance and inductance of PSPN coils under strain (Fig. 3c and Supplementary Fig. 19) and bending (Supplementary Fig. 20).

Accordingly, we experimentally measured the variations of scattering parameters $S_{11}$ and $S_{21}$, and the transfer efficiency $\eta$ of the WPT system across uniaxial strains (Fig. 3d–f). We note a slight change in these parameters for up to 100% strain. In addition, Advanced Design System simulation indicates the strain-insensitive feature of the induced voltage on the stretchable PSPN coil (Fig. 3f, inset). The extracted transfer efficiency of the stretchable WPT system at 50 MHz reduces slightly from 76.0% to 74.8% at 50% strain and further to 66.6% at 100% strain (Fig. 3g). This arises primarily from the altered coupling strength caused by geometry changes between the two coils. Notably, our device outperformed an Ag-NW-nanofibre-based antenna[50]. Conversely, the coils' efficiency with the non-porous composite dropped sharply to 23.1% at 25% strain, with a total loss of power transfer capability by 50% strain (Fig. 3g and Supplementary Fig. 21). As anticipated, a shorter distance between the coils notably boosts transfer efficiency (Fig. 3h).

NFC-based wireless powering and data transmission systems enable a myriad of new applications for wearable and implantable bioelectronic devices[48,51,52]. These devices, however, rely on intrinsically

https://doi.org/10.1038/s41565-024-01658-6

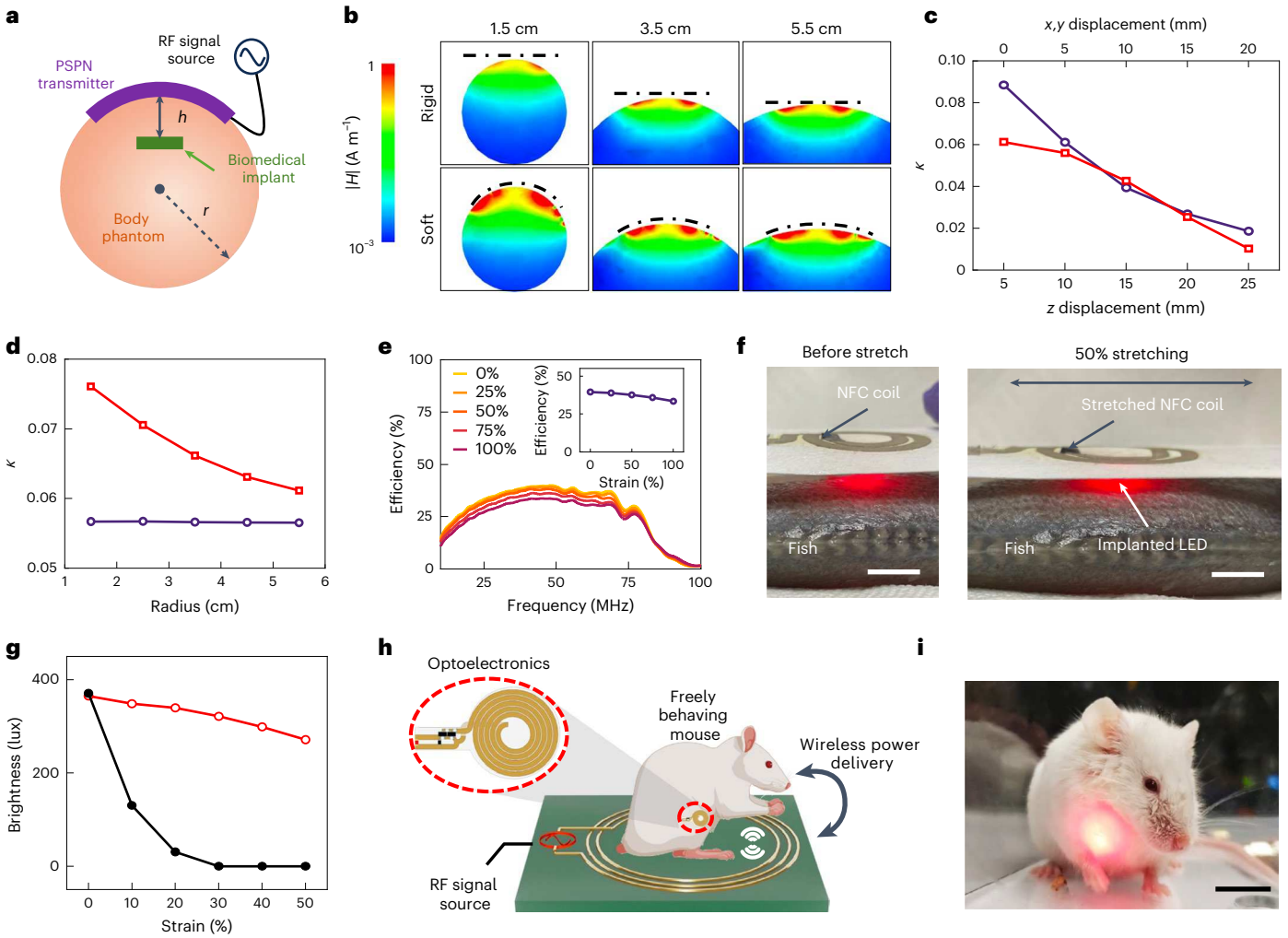


**Fig. 4 | Stretchable wireless powering system for wearable and implantable bioelectronics. a**,**b**, Schematic of a simplified structure (**a**) and Maxwell simulations (**b**) of the magnetic field generated by a rigid (top) and soft transmitter (bottom) placed on various body parts with diameters of 1.5, 3.5 and 5.5 cm. Dotted lines represent the transmitter coils used for the simulation. **c**, Coupling coefficient between the soft transmitter and implanted receiver coils with varied lateral (*x*,*y*, red) and vertical (*z*, blue) distances. **d**, Coupling coefficient between the soft PSPN (red) or rigid (blue) transmitter coil and the implanted receiver coil with varied phantom radii ($h = 1$ cm). **e**, Transfer efficiency of the WPT system comprising the stretchable PSPN transmitter and implanted receiver, as a function of tensile strain. Inset: extracted efficiency at 50 MHz, indicating the strain-insensitive performance for up to 50% strain. Here the phantom radius is 5.5 cm, and the implantation depth is 1 cm. The coloured lines represent various tensile strains. **f**, Photographs of a stretchable wireless powering system. A stretchable transmitter coil made of PSPN was used to power a red LED device implanted in fish, demonstrating robust and reliable operation when stretched at 50% strain. Scale bars, 2 cm. **g**, Quantitative brightness of the LED wirelessly powered by a transmitter made of PSPN (red) and conventional Ag NWs (black) under strain. **h**, Schematic illustration of the in vivo demonstration for the implantable WPT system. An implantable optoelectronic device is subcutaneously implanted between the skin and muscle on the ventral side of the animal. The transmitter wirelessly delivers RF power to the implanted optoelectronic device with precise control over its operation, while allowing for unrestricted movement of the animal. **i**, Photograph of an implanted mouse freely behaving in an NFC-powered set-up. Scale bar, 2 cm.

rigid materials with limited stretchability (<30%), which falls short of meeting the strain-tolerance requirement for certain skin-interfaced devices (>80%)[53]. We fabricated wearable wireless power transmitters and implantable receivers based on PSPN. We first theoretically evaluated the transmitter coil's performance to power a device implanted in a body phantom, constructed from a glass cylinder filled with 1% agarose gel (Fig. 4a and Supplementary Fig. 22). Electromagnetic simulations reveal that the inherently soft nanocomposite coil seamlessly adapts to curved body contours. This adaptability facilitates deeper penetration of electromagnetic power into the body, resulting in superior power delivery compared with its rigid counterparts (Fig. 4b and Supplementary Fig. 23). Experiments reveal that the coupling coefficient $\kappa$ diminishes with increasing lateral and vertical separation between the coils (Fig. 4c). Moreover, the soft conformal coil exhibits higher coupling coefficients than conventional rigid coil at all radii (Fig. 4d). Additionally, we note that the transfer efficiency (radius, 5.5 cm; implantation depth, 1 cm) remains stable (>33%) at 50 MHz within 100% tensile strain (Fig. 4e). To evaluate the wireless powering further, we used the PSPN transmitter coil to power an implanted red light-emitting diode (LED) in fish (Fig. 4f). Quantitative analysis of the LED brightness suggests reliable and stable operation of the PSPN coil at 50% strain. In contrast, the conventional Ag NW coil degrades rapidly upon stretching, failing electrically at just 20% strain (Fig. 4g).

To further explore PSPN's potential as an implantable receiver coil, we developed a wireless optoelectronic system comprising an implantable energy-harvesting device that captures an RF signal from an external transmitter, processes the signal through a voltage multiplier, and subsequently routes the generated d.c. voltage to illuminate

https://doi.org/10.1038/s41565-024-01658-6

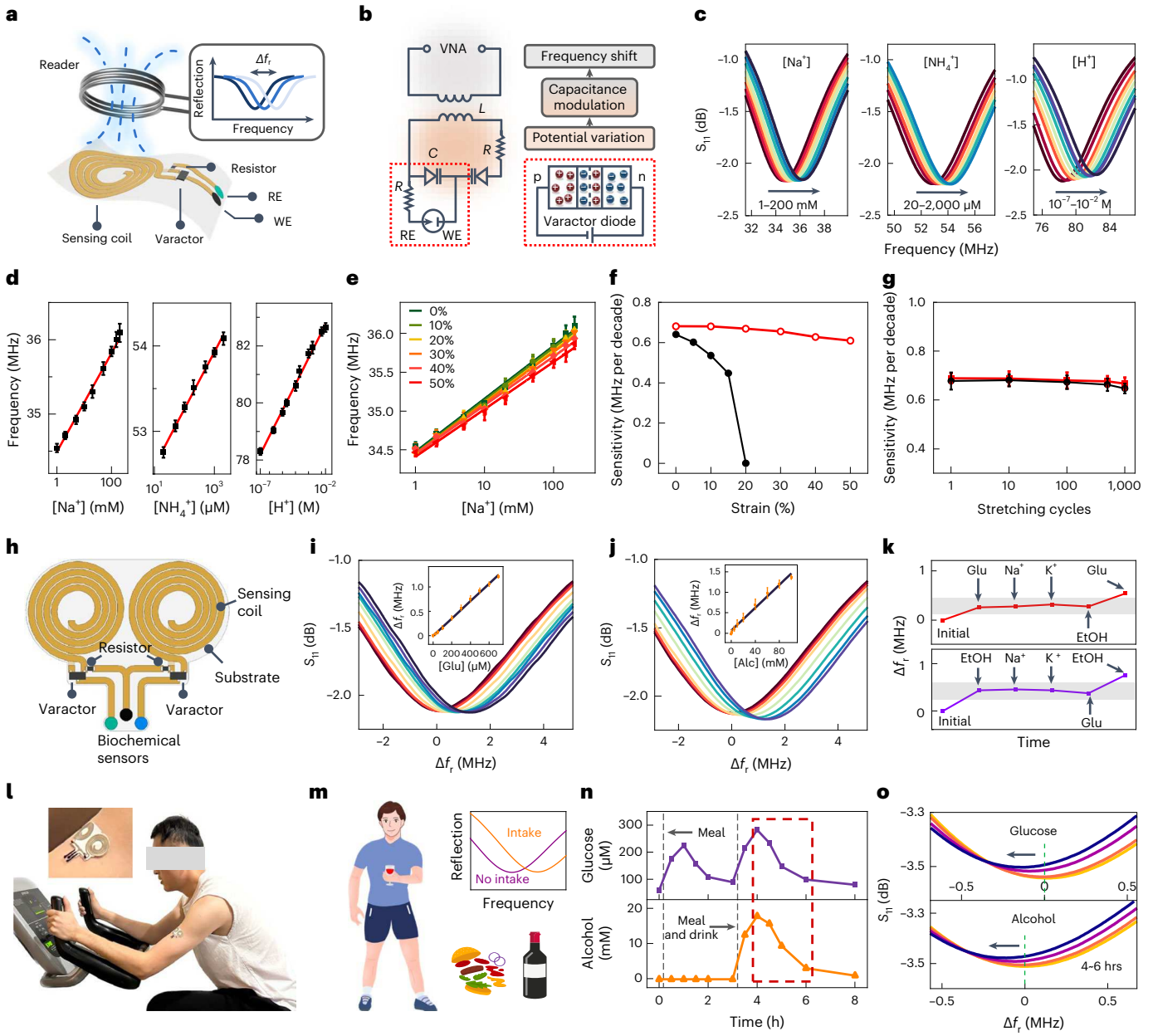


**Fig. 5 | Wireless stretchable bioelectronics for multiplexed biochemical sensing. a**, Schematic illustration of the stretchable, battery-free and wireless inductor–capacitor-circuit-based bioelectronics for biochemical sensing. RE, reference electrode; WE, working electrode. **b**, Equivalent circuit and operating principle of the wireless sensing system. **c**,**d**, Reflection coefficients (**c**) and frequency shifts (**d**) for wireless $Na^+$ (1–200 mM), $NH_4^+$ (20–2,000 μM) and $H^+$ ($10^{-7}$–$10^{-2}$ M) monitoring. **e**,**f**, Frequency shifts (**e**) and sensitivity (**f**) of the wireless $Na^+$ sensing system made of PSPN (red) and conventional Ag NWs (black) under strain. The coloured lines in **e** represent various tensile strains. **g**, Alterations in sensitivity observed in the $Na^+$ sensing system after subjecting the PSPN device to 1,000 repetitive stretching cycles at strain levels of 25% (red) and 50% (black). **h**, Schematic of wireless on-body stretchable bioelectronics for multiplexed biochemical sensing. **i**,**j**, Reflection coefficients for wireless on-body glucose (**i**) and alcohol (**j**) monitoring. Insets: calibration plots. **k**, Selectivity tests of the multiplexed sensing system. Glucose (top) and alcohol (bottom) sensor responses to the addition of target molecules and interfering biomarkers, including glucose (150 μM), $Na^+$ (20 mM), $K^+$ (5 mM) and ethanol (20 mM). **l**, Photograph of a volunteer wearing a multiplexed wireless biochemical sensing system during cycling exercise. **m**–**o**, Illustration (**m**) and dynamic wireless analysis of sweat glucose and ethanol levels (**n**,**o**) with and without intake of food and drink over the course of 8 h. Sweat secretion was triggered by a 10 min session of constant-load stationary cycling. Raw data from 4 to 6 h in **n** (red dashed box) are depicted in **o**. Error bars in **d**,**e**,**g**,**i**,**j** represent the s.d. of the mean from three samples.

a red LED (Supplementary Fig. 24). We encapsulated the device with silicone elastomer (Smooth-on) and placed it between the skin and muscle (subcutaneously) on the ventral side of a mouse under isoflurane anaesthesia (Fig. 4h). There was negligible degradation of the device when stored in phosphate-buffered saline (PBS; pH 7.4) and in artificial perspiration (pH 4.3, Pickering Laboratories) for 9 days at room temperature (Supplementary Fig. 25). The WPT thus enables real-time, precise control of illumination for freely moving mice (Fig. 4i and Supplementary Videos 3 and 4).

## Wireless and multiplexed biochemical sensing

Furthermore, we fabricated a fully stretchable wireless bioelectronic system for multiplexed biochemical sensing. Our battery-free bioelectronic platform comprises a stretchable biochemical sensing interface

and a spiral coil as the coupling unit for wireless data transmission (Fig. 5a). The design principle relies on a modularized inductor–capacitor resonance circuit model where varactors convert electrical potential variations into capacitance modulations (Fig. 5b). These modulations directly correspond with the resonance frequency $f_r$ of the inductor–capacitor circuit, as described by:

$$f_r = \frac{1}{2\pi\sqrt{LC}}$$

where $L$ and $C$ are the equivalent inductance and capacitance of the resonance circuit, respectively. When targeted analytes are present, the potential difference between the working and reference electrodes of the biochemical sensors corresponds to a frequency shift. Since $f_r$ is an intrinsic property of the resonance circuit, it allows for robust and reliable wireless data transmission. This was exemplified by high-fidelity measurement of a wealth of ions, including $Na^+$, $K^+$, $NH_4^+$ and $H^+$ (Fig. 5c,d and Supplementary Fig. 26). The obtained readouts exhibit a linear relationship with high sensitivities of 0.66, 0.61, 0.67 and 1.04 MHz per decade, respectively. To achieve multiplexed sensing of biomarkers to capture biometric signature profiles with a minimum level of crosstalk, we carefully chose capacitors in the resonance circuit, producing distinct resonance dips at approximately 38, 55 and 80 MHz. Varying a single analyte in the solution primarily affects its corresponding $f_r$, with minimal shifts in other sensors, highlighting remarkable selectivity against interfering ions (Supplementary Fig. 27).

When the PSPN sensing device was subjected to uniaxial tensile stretch, a strain insensitivity of less than 10% performance variation is observed when stretched up to 50% strain, that is, from 0.68 to 0.62 MHz per decade (Fig. 5e,f). Such changes largely stem from alterations in the device geometry, which weaken the coupling strength. Conversely, the device made of conventional non-porous Ag NWs exhibited stark instability under strain, causing a sensitivity reduction from 0.64 to 0.45 MHz per decade at 15% and becoming non-operational at 20% (Fig. 5f and Supplementary Fig. 28). Furthermore, the devices maintained their initial performance across repetitive strain cycles, with only ~3% and ~5% sensitivity changes after 1,000 cycles at 25% and 50% strains, respectively (Fig. 5g).

We constructed a multiplexed wireless sensing system integrating glucose and alcohol sensors with high sensitivities of 1.79 and 0.014 MHz $mM^{-1}$ respectively (Fig. 5h–j). These developed sensors showcased minimal signal fluctuations even when introduced to a range of interfering biomarkers (Fig. 5k and Supplementary Fig. 29). Notably, our wireless sensing system remains stable at physiologically relevant temperatures (Supplementary Fig. 30). Our wireless sensor prototype forms an intimate interface with human skin due to the absence of on-chip integrated circuits (Fig. 5l). This battery-free device facilitates continuous, real-time perspiration monitoring during everyday activities (Fig. 5m). For example, we monitored the evolution of glucose and ethanol concentrations in perspiration over the course of 8 h. We observed a notable rise and subsequent rapid decline in glucose levels—with alcohol levels remaining largely unchanged—post the first meal between 0 and 3 h (Fig. 5n). Furthermore, the two biomarkers exhibited nearly synchronized variations following a combined intake of a meal and a drink (1.2 g of white wine (50% alcohol by volume) per 1 kg of the volunteer's body weight) (Fig. 5n,o).

## Conclusions

We also note that the phase-separation technique can be potentially extended to other conductive nanofillers, such as carbon nanotubes (Supplementary Fig. 31). These findings suggest that the phase-separation approach could open up new avenues for constituent materials across diverse domains. Future research should focus on exploring new manufacturing technologies (for example, additive manufacturing) that are compatible with this technique to enable scalable production. The development of strain-insensitive, NFC-based wireless bioelectronics with customized biosensing and therapeutic modules holds promise for a variety of healthcare applications.

## Online content

Any methods, additional references, Nature Portfolio reporting summaries, source data, extended data, supplementary information, acknowledgements, peer review information; details of author contributions and competing interests; and statements of data and code availability are available at https://doi.org/10.1038/s41565-024-01658-6.

## References


1. Jung, D. et al. Highly conductive and elastic nanomembrane for skin electronics. *Science* **373**, 1022–1026 (2021).
2. Choi, S. et al. Highly conductive, stretchable and biocompatible Ag–Au core–sheath nanowire composite for wearable and implantable bioelectronics. *Nat. Nanotechnol.* **13**, 1048–1056 (2018).
3. Lee, W. et al. Universal assembly of liquid metal particles in polymers enables elastic printed circuit board. *Science* **378**, 637–641 (2022).
4. Matsuhisa, N. et al. Printable elastic conductors by in situ formation of silver nanoparticles from silver flakes. *Nat. Mater.* **16**, 834–840 (2017).
5. Veerapandian, S. et al. Hydrogen-doped viscoplastic liquid metal microparticles for stretchable printed metal lines. *Nat. Mater.* **20**, 533–540 (2021).
6. Hui, Y. et al. Three-dimensional printing of soft hydrogel electronics. *Nat. Electron.* **5**, 893–903 (2022).
7. Jiang, Z. et al. A 1.3-micrometre-thick elastic conductor for seamless on-skin and implantable sensors. *Nat. Electron.* **5**, 784–793 (2022).
8. Zhao, Y. et al. A self-healing electrically conductive organogel composite. *Nat. Electron.* **6**, 206–215 (2023).
9. Jiang, Z. et al. Highly stretchable metallic nanowire networks reinforced by the underlying randomly distributed elastic polymer nanofibers via interfacial adhesion improvement. *Adv. Mater.* **31**, 1903446 (2019).
10. Luo, Y. et al. Technology roadmap for flexible sensors. *ACS Nano* **17**, 5211–5295 (2023).
11. Wang, C., He, T., Zhou, H., Zhang, Z. & Lee, C. Artificial intelligence enhanced sensors—enabling technologies to next-generation healthcare and biomedical platform. *Bioelectron. Med.* **9**, 17 (2023).
12. Choi, S., Han, S. I., Kim, D., Hyeon, T. & Kim, D.-H. High-performance stretchable conductive nanocomposites: materials, processes, and device applications. *Chem. Soc. Rev.* **48**, 1566–1595 (2019).
13. Sim, K., Rao, Z., Ershad, F. & Yu, C. Rubbery electronics fully made of stretchable elastomeric electronic materials. *Adv. Mater.* **32**, 1902417 (2020).
14. Gao, W. et al. Fully integrated wearable sensor arrays for multiplexed in situ perspiration analysis. *Nature* **529**, 509–514 (2016).
15. Yang, Y. & Gao, W. Wearable and flexible electronics for continuous molecular monitoring. *Chem. Soc. Rev.* **48**, 1465–1491 (2019).
16. Kim, J. J. et al. Skin electronics: next-generation device platform for virtual and augmented reality. *Adv. Funct. Mater.* **31**, 2009602 (2021).
17. Yamagishi, K., Zhou, W., Ching, T., Huang, S. Y. & Hashimoto, M. Ultra-deformable and tissue-adhesive liquid metal antennas with high wireless powering efficiency. *Adv. Mater.* **33**, 2008062 (2021).
18. Zhuang, Q. et al. Wafer-patterned, permeable, and stretchable liquid metal microelectrodes for implantable bioelectronics with chronic biocompatibility. *Sci. Adv.* **9**, eadg8602 (2023).

19. Jung, D. et al. Adaptive self-organization of nanomaterials enables strain-insensitive resistance of stretchable metallic nanocomposites. *Adv. Mater.* **34**, 2200980 (2022).
20. Wang, T., Liu, Q., Liu, H., Xu, B. & Xu, H. Printable and highly stretchable viscoelastic conductors with kinematically reconstructed conductive pathways. *Adv. Mater.* **34**, 2202418 (2022).
21. Kim, S. H. et al. An ultrastretchable and self-healable nanocomposite conductor enabled by autonomously percolative electrical pathways. *ACS Nano* **13**, 6531–6539 (2019).
22. Sun, B. et al. Gas-permeable, multifunctional on-skin electronics based on laser-induced porous graphene and sugar-templated elastomer sponges. *Adv. Mater.* **30**, 1804327 (2018).
23. Yi, H. et al. Constructing high-performance 3D porous self-standing electrodes with various morphologies and shapes by a flexible phase separation-derived method. *J. Mater. Chem. A* **7**, 22550–22558 (2019).
24. Wang, Y., Yokota, T. & Someya, T. Electrospun nanofiber-based soft electronics. *NPG Asia Mater.* **13**, 22 (2021).
25. Zhu, D., Handschuh-Wang, S. & Zhou, X. Recent progress in fabrication and application of polydimethylsiloxane sponges. *J. Mater. Chem. A* **5**, 16467–16497 (2017).
26. Yao, S. et al. Ultrasoft porous 3D conductive dry electrodes for electrophysiological sensing and myoelectric control. *Adv. Mater. Technol.* **7**, 2101637 (2022).
27. Zhou, W. et al. Gas-permeable, ultrathin, stretchable epidermal electronics with porous electrodes. *ACS Nano* **14**, 5798–5805 (2020).
28. Wang, F. et al. Progress report on phase separation in polymer solutions. *Adv. Mater.* **31**, 1806733 (2019).
29. Hołda, A. K. & Vankelecom, I. F. Understanding and guiding the phase inversion process for synthesis of solvent resistant nanofiltration membranes. *J. Appl. Polym. Sci.* **132**, 42130 (2015).
30. Mandal, J. et al. Hierarchically porous polymer coatings for highly efficient passive daytime radiative cooling. *Science* **362**, 315–319 (2018).
31. Zhu, H.-W. et al. Printable elastic silver nanowire-based conductor for washable electronic textiles. *Nano Res.* **13**, 2879–2884 (2020).
32. Lee, H. J., Jung, B., Kang, Y. S. & Lee, H. Phase separation of polymer casting solution by nonsolvent vapor. *J. Membr. Sci.* **245**, 103–112 (2004).
33. Sun, X., Sun, G. & Wang, X. Morphology modeling for polymer monolith obtained by non-solvent-induced phase separation. *Polymer* **108**, 432–441 (2017).
34. Binks, B. & Lumsdon, S. Pickering emulsions stabilized by monodisperse latex particles: effects of particle size. *Langmuir* **17**, 4540–4547 (2001).
35. Hu, N., Karube, Y., Yan, C., Masuda, Z. & Fukunaga, H. Tunneling effect in a polymer/carbon nanotube nanocomposite strain sensor. *Acta Mater.* **56**, 2929–2936 (2008).
36. Amjadi, M., Pichitpajongkit, A., Lee, S., Ryu, S. & Park, I. Highly stretchable and sensitive strain sensor based on silver nanowire–elastomer nanocomposite. *ACS Nano* **8**, 5154–5163 (2014).
37. Li, J. et al. Correlations between percolation threshold, dispersion state, and aspect ratio of carbon nanotubes. *Adv. Funct. Mater.* **17**, 3207–3215 (2007).
38. Taherian, R. Development of an equation to model electrical conductivity of polymer-based carbon nanocomposites. *ECS J. Solid State Sci. Technol.* **3**, M26–M38 (2014).
39. Liu, Y. et al. Capillary-force-induced cold welding in silver-nanowire-based flexible transparent electrodes. *Nano Lett.* **17**, 1090–1096 (2017).
40. Zheng, X. et al. Ultralight, ultrastiff mechanical metamaterials. *Science* **344**, 1373–1377 (2014).
41. Liu, S., Rao, Y., Jang, H., Tan, P. & Lu, N. Strategies for body-conformable electronics. *Matter* **5**, 1104–1136 (2022).
42. Kim, Y. et al. Stretchable nanoparticle conductors with self-organized conductive pathways. *Nature* **500**, 59–63 (2013).
43. Boland, C. S. et al. Sensitive electromechanical sensors using viscoelastic graphene–polymer nanocomposites. *Science* **354**, 1257–1260 (2016).
44. Sun, H., Han, Z. & Willenbacher, N. Ultrastretchable conductive elastomers with a low percolation threshold for printed soft electronics. *ACS Appl. Mater. Interfaces* **11**, 38092–38102 (2019).
45. Liu, Y., Ji, X. & Liang, J. Rupture stress of liquid metal nanoparticles and their applications in stretchable conductors and dielectrics. *Npj Flex. Electron.* **5**, 11 (2021).
46. Ma, Z. et al. Permeable superelastic liquid-metal fibre mat enables biocompatible and monolithic stretchable electronics. *Nat. Mater.* **20**, 859–868 (2021).
47. Chung, H. U. et al. Binodal, wireless epidermal electronic systems with in-sensor analytics for neonatal intensive care. *Science* **363**, eaau0780 (2019).
48. Ouyang, W. et al. A wireless and battery-less implant for multimodal closed-loop neuromodulation in small animals. *Nat. Biomed. Eng.* **7**, 1252–1269 (2023).
49. Jiang, Y. et al. Wireless, closed-loop, smart bandage with integrated sensors and stimulators for advanced wound care and accelerated healing. *Nat. Biotechnol.* **41**, 652–662 (2023).
50. Zhang, Y. et al. High precision epidermal radio frequency antenna via nanofiber network for wireless stretchable multifunction electronics. *Nat. Commun.* **11**, 5629 (2020).
51. Liu, T.-L. et al. Battery-free, tuning circuit–inspired wireless sensor systems for detection of multiple biomarkers in bodily fluids. *Sci. Adv.* **8**, eabo7049 (2022).
52. Park, S. I. et al. Soft, stretchable, fully implantable miniaturized optoelectronic systems for wireless optogenetics. *Nat. Biotechnol.* **33**, 1280–1286 (2015).
53. Someya, T., Bao, Z. & Malliaras, G. G. The rise of plastic bioelectronics. *Nature* **540**, 379–385 (2016).




[1]Department of Chemical and Biomedical Engineering, University of Missouri, Columbia, MO, USA. [2]Andrew and Peggy Cherng Department of Medical Engineering, Division of Engineering and Applied Science, California Institute of Technology, Pasadena, CA, USA. [3]Department of Electrical and Computer Engineering, University of Illinois at Chicago, Chicago, IL, USA. [4]Department of Mechanical and Aerospace Engineering, University of Missouri, Columbia, MO, USA. [5]Department of Surgery-Transplant and Mary and Dick Holland Regenerative Medicine Program, University of Nebraska Medical Center, Omaha, NE, USA. [6]Materials Science and Engineering Institute, University of Missouri, Columbia, MO, USA. [7]NextGen Precision Health, University of Missouri, Columbia, MO, USA. [8]These authors contributed equally: Yadong Xu, Zhilu Ye, Ganggang Zhao. ✉e-mail: weigao@caltech.edu; pychen@uic.edu; yanzheng@missouri.edu

## Methods

Our research complies with all relevant ethical regulations. Specifically, all animal procedures were performed in accordance with the National Institutes of Health Guide for the Care and Use of Laboratory Animals and were approved by the University of Missouri Animal Care and Use Committee. The on-body evaluations of skin-interfaced devices on human participants were conducted under approval from Institutional Review Board at the University of Missouri-Columbia (number 2010272). All human subjects gave written and informed consent before participation in the studies. The healthy participant (age 28 years; male) was recruited from the University of Missouri campus through word of mouth.

### Materials

Bis(2-ethylehexyl) sebacate (DOS), 1-butanol, sodium tetrakis [3,5-bis(trifluoromethyl)phenyl] borate (Na-TFPB), polyvinyl chloride (PVC), sodium tetraphenylborate (NaTPB), cyclohexanone, polyvinyl butyral (BUTVAR B-98, PVB), $NH_4^+$ ionophore (nonactin), alcohol oxidase, bovine serum albumin, NaCl, KCl and $NH_4Cl$ were purchased from Sigma Aldrich. Polyaniline base, acetic acid, dimethyl sulfoxide (DMSO), THF, cyclohexanone, PBS solution and dextrose (D-glucose) were obtained from Fisher Scientific. Glucose oxidase was acquired from Toyobo. Ag/AgCl ink was purchased from CH Instruments.

### Synthesis of PSPN and device fabrications

The phase-separated porous Ag NW nanocomposites were prepared by mixing PU (Texin RxT85A, Covestro) solution (in THF) with Ag NW solution (20 mg $ml^{-1}$ in ethanol; Ag NW-40, ACS Material) at various concentrations and volume ratios. Drop-casting the nanocomposite precursor solution on aluminium foils and drying under ambient conditions (~3 h) completed the fabrication of highly conductive PSPN film. Note that the electrical conductivity, stretchability and electrical-mechanical decoupling are tunable based on the concentrations and volume ratios of constituent materials. PSPN denotes PSPN made from ethanol-based Ag NW solution, whereas PSPN with 1-butanol represents that made with the co-addition of 1-butanol to control pore size (Supplementary Fig. 4). The optimum porous nanocomposite was prepared by mixing 5 g of PU solution (90 mg $ml^{-1}$) with 4.5 ml of Ag NW solution (20 mg $ml^{-1}$) and was used throughout the study unless otherwise stated. Similarly, porous PU substrates were also fabricated by mixing 50 ml of PU solution (70 mg $ml^{-1}$ in THF) with 40 ml of 1-butanol and dried under ambient conditions. The non-porous Ag NW nanocomposite was fabricated by mixing PU (HydroMed D3, AdvanSource Biomaterial) solution (ethanol:water, 9:1) with Ag NW solution (20 mg $ml^{-1}$ in ethanol). Conventional Ag NWs were fabricated by spray-coating Ag NWs onto oxygen-plasma-treated elastomeric PU substrate. Laser cutting using a VLS2.30 universal laser system defines the desired patterns. The stretchable wireless NFC antenna was obtained by transferring predesigned spiral PSPN coils, assisted by Aquasol water-soluble tape, to the porous PU substrates. Waterborne PU adhesive (HydroMed D3, AdvanSource Biomaterial) allows for a strong and robust interface under strain between PSPN and the substrate.

### Fabrication of biochemical sensors

We first fabricated soft and stretchable sensors (3 mm diameter) by transfer-printing of laser-induced graphene (LIG) electrodes onto PU elastomer substrates. Specifically, the LIG electrodes were engraved on a polyimide film using a 30 W $CO_2$ laser cutter (power, 12%; speed, 15%; VLS2.30 universal laser systems). Next, PU solution (Texin RxT85A, 40 mg $ml^{-1}$ in THF) was applied and dried at room temperature. Careful transfer-printing from polyimide film to PU elastomer completed the process. The sodium ion sensor was prepared by drop-casting 10 µl of $Na^+$-selective membrane solution (1 mg of Na ionophore, 0.55 mg of Na-TFPB, 33 mg of PVC and 65.45 mg of DOS in 660 µl of THF) on the graphene electrode. The potassium sensor was prepared by drop-casting 6 µl of $K^+$-selective membrane solution (2 mg of valinomycin, 0.5 mg of NATPB, 32.7 mg of PVC and 64.7 mg of DOS in 350 µl of cyclohexanone) on each LIG electrode. The $NH_4^+$ sensor was fabricated by drop-casting 6 µl of $NH_4^+$-selective membrane solution (1 mg of $NH_4^+$ ionophore (nonactin), 33 mg of PVC and 66 mg of DOS in THF) on the LIG electrode. Next, the pH sensor was prepared by drop-casting 10 µl of the polyaniline base solution (20 mg $ml^{-1}$ in DMSO) on the LIG electrode and dried at 80 °C, followed by 15 min of incubation in 1.0 M HCl. To prepare enzyme-based sensors, gold nanoparticles (25 nm) was first sputter-coated on the LIG electrodes, and 5 µl of cocktail (10 mg of Prussian blue and 5 mg of chitosan dissolved in 1 ml of 0.1 M acetic acid) was then drop-cast. Next, 5 µl of enzyme solution was added and dried at 4 °C overnight, followed by addition of 3 µl of 0.5% Nafion solution. Here, the glucose oxidase solution was prepared by mixing glucose oxidase (10 mg $ml^{-1}$ in PBS) with chitosan/carbon nanotube solution (1% chitosan and 5 mg $ml^{-1}$ of multiwalled carbon nanotube in 0.1 M acetic acid) at a volume ratio of 1:1. The alcohol oxidase solution was composed of alcohol oxidase, bovine serum albumin (10 mg $ml^{-1}$ in PBS) and chitosan (1% in 0.1 M acetic acid) with a volume ratio of 8:1:1. The reference electrode was prepared by first applying a layer of Ag/AgCl paste onto the LIG electrode, followed by the addition of 3 µl of PVB solution (79.1 mg of PVB and 50 mg of NaCl in 1 ml of methanol).

### Characterizations and measurements

Scanning electron microscopy (SEM) images were taken with a FEI Quanta 600 FEG Environmental SEM. WVTRs were determined based on ASTM96 at 35 °C. Mechanical properties were characterized using a Mark-10 ESM303 tensile tester. Electrical conductance was measured by a digital source meter (2604B, Keithley Instruments). Fourier transform infrared spectra were obtained using a Nicolet 6700 spectrometer (Thermo Electron). Electrocardiogram signals were recorded with a PowerLab T26 (AD Instruments). Statistical analyses were carried out using Origin 2016 software.

### Coil design and numerical simulations

The spiral coils for wearable WPT applications (Figs. 3 and 4b–g and Supplementary Figs. 19–23) were custom-designed with an 8 mm inner radius, two turns, 5 mm trace width and 1 mm spacing. The implantable receiver coils (Fig. 4h,i and Supplementary Fig. 24) feature a 5.5 mm inner radius, five turns, 1.5 mm trace width and 0.3 mm spacing. The sensing coils for monitoring ions and metabolites (Fig. 5) are characterized by a 4 mm inner radius, four turns, 1.5 mm trace width and 0.3 mm spacing. The magnetic field distributions for the WPT system (Fig. 3a), the coil under strain (Fig. 3b) and the coil placed on the human body (Fig. 4b and Supplementary Fig. 23) were simulated by using Ansys Maxwell. In particular, for Fig. 4b and Supplementary Fig. 23, the human body was modelled by a stratified composition of a 1 mm skin layer with relative permittivity of 43 and relative permeability of 1, a 2 mm adipose layer with relative permittivity of 5.28 and relative permeability of 1, and a 7 mm bone layer with relative permittivity of 11.4 and relative permeability of 1. Notably, due to the unit permeability of those materials, the presence of human tissue barely affects the performance of the WPT system. The RF system simulations (Fig. 3f, inset) were performed by Advanced Design System.

**RF properties characterization and measurements.** The equivalent inductance ($L$), resistance ($R$) and $Q$-factor of the coil were obtained by directly connecting the coil to a vector network analyser (VNA; N5242B PNA-X Network Analyzer, Keysight) and measuring the input impedance $Z_{in}$. The $L$, $R$ and $Q$ values could be extracted from $Z_{in}$ according to the following equation:

$$L = \frac{\mathrm{Im}(Z_{in})}{2\pi f}$$

$$R = \mathrm{Re}(Z_{\mathrm{in}})$$

$$Q = \frac{\mathrm{Im}(Z_{\mathrm{in}})}{\mathrm{Re}(Z_{\mathrm{in}})} = \frac{2\pi fL}{R}$$

where $\mathrm{Im}(Z_{\mathrm{in}})$ and $\mathrm{Re}(Z_{\mathrm{in}})$ are the imaginary and real parts of the input impedance $Z_{\mathrm{in}}$, respectively, and $f$ is the frequency. For WPT applications, the scattering parameters ($S_{11}$ and $S_{21}$) and impedance parameters ($Z_{11}$, $Z_{12}$ and $Z_{22}$) of the two-port network were also measured by the Keysight PNA-X VNA. The power transfer efficiency $\eta$ could be derived from the scattering parameters and the coupling coefficient $\kappa$ could be obtained from the impedance parameters. The brightness of the LED for demonstrating the power transfer efficiency was measured by a light meter (ET130, Klein Tools). A portable VNA (LibreVNA) was used for continuous, real-time perspiration monitoring. Common-cathode varactors MAVR-000409-0287FT, MAVR-000405-0287FT and MAVR-045441-0287AT (Macom) were used to achieve resonances at around 38, 55 and 80 MHz, respectively. The power transfer efficiency $\eta$ is given by:

$$\eta = \frac{|S_{21}|^2}{1 - |S_{11}|^2}$$

where $S_{21}$ and $S_{11}$ are the transmission and reflection coefficients of the two-port network. The coupling coefficient, $\kappa$, representing the fraction of magnetic flux between the transmitter and receiver coils, is given by

$$\kappa = \frac{M}{\sqrt{L_1 L_2}} = \frac{\mathrm{Im}(Z_{12})}{\sqrt{\mathrm{Im}(Z_{11})\mathrm{Im}(Z_{22})}},$$

where $M$ is the mutual inductance between the two coils, and $\mathrm{Im}(Z_{11})$, $\mathrm{Im}(Z_{12})$ and $\mathrm{Im}(Z_{22})$ are the imaginary components of the two-port network's impedance parameters.

### Implantation of stretchable wireless optoelectronic device

Adult female Swiss Webster mice (10–14 weeks old, Charles River) were used for surgical implantation of the device. Mice were group housed in cages (20–26 °C, 30–70% humidity) on a 12 h/12 h light/dark cycle and fed a standard chow diet ad libitum. The whole device was first sterilized using ethanol, and then implanted between the skin and muscle (subcutaneously) on the ventral side of the animal under isoflurane anaesthesia. Prior to implantation, a small incision was made on the lateral side of the animal and the skin was separated from the abdominal muscle with blunt forceps. After implantation, skin was closed with sutures and the animal was allowed to recover from anaesthesia.

### Reporting summary

Further information on research design is available in the Nature Portfolio Reporting Summary linked to this article.

## Data availability

The main data supporting the results in this study are available within the paper and its Supplementary Information. Source data for Figs. 1–5 are provided with this paper. Source data are provided with this paper.

## Acknowledgements

Z. Yan acknowledges financial support from the start-up fund of the University of Missouri-Columbia. Z. Yan, P.-Y.C. and J.X. acknowledge the National Institute of Biomedical Imaging and Bioengineering (award number R01EB033371). The human study was supported by Z. Yan's start-up fund. W.G. acknowledges support from National Institutes of Health grants (R01HL155815 and R21DK13266). P.-Y.C. acknowledges financial support from NSF ECCS 2229659. I.O. acknowledges financial support from the start-up fund of the University of Missouri-Columbia.

## Author contributions

Z. Yan, Y.X., P.-Y.C. and Z. Ye conceived the idea and led research efforts. Y.X., Z. Ye, G.Z., Q.F., Z.C., J.L., M.Y., Y.R., Y.L., X.Q., L.S. and J.X. performed the experiments. J.L. conducted numerical simulations. I.O. and B.B. led animal studies and performed surgeries. Z. Yan, Y.X., Z. Ye and W.G. wrote the paper with assistance of the other coauthors.

## Competing interests

The authors declare no competing interests.

## Additional information

**Supplementary information** The online version contains supplementary material available at https://doi.org/10.1038/s41565-024-01658-6.

**Correspondence and requests for materials** should be addressed to Wei Gao, Pai-Yen Chen or Zheng Yan.

**Peer review information** *Nature Nanotechnology* thanks Michael Dickey, Chengkuo Lee and Xuechang Zhou for their contribution to the peer review of this work.

nature portfolio

Corresponding author(s): Wei Gao
Pai-Yen Chen
Zheng Yan

Last updated by author(s): Mar 10, 2024

# Reporting Summary

Nature Portfolio wishes to improve the reproducibility of the work that we publish. This form provides structure for consistency and transparency in reporting. For further information on Nature Portfolio policies, see our Editorial Policies and the Editorial Policy Checklist.

## Statistics

For all statistical analyses, confirm that the following items are present in the figure legend, table legend, main text, or Methods section.

| n/a | Confirmed | |
|---|---|---|
| ☐ | ☒ | The exact sample size (*n*) for each experimental group/condition, given as a discrete number and unit of measurement |
| ☐ | ☒ | A statement on whether measurements were taken from distinct samples or whether the same sample was measured repeatedly |
| ☒ | ☐ | The statistical test(s) used AND whether they are one- or two-sided<br>*Only common tests should be described solely by name; describe more complex techniques in the Methods section.* |
| ☒ | ☐ | A description of all covariates tested |
| ☒ | ☐ | A description of any assumptions or corrections, such as tests of normality and adjustment for multiple comparisons |
| ☐ | ☒ | A full description of the statistical parameters including central tendency (e.g. means) or other basic estimates (e.g. regression coefficient) AND variation (e.g. standard deviation) or associated estimates of uncertainty (e.g. confidence intervals) |
| ☒ | ☐ | For null hypothesis testing, the test statistic (e.g. *F*, *t*, *r*) with confidence intervals, effect sizes, degrees of freedom and *P* value noted<br>*Give P values as exact values whenever suitable.* |
| ☒ | ☐ | For Bayesian analysis, information on the choice of priors and Markov chain Monte Carlo settings |
| ☒ | ☐ | For hierarchical and complex designs, identification of the appropriate level for tests and full reporting of outcomes |
| ☒ | ☐ | Estimates of effect sizes (e.g. Cohen's *d*, Pearson's *r*), indicating how they were calculated |

*Our web collection on statistics for biologists contains articles on many of the points above.*

## Software and code

Policy information about availability of computer code

| | |
|---|---|
| Data collection | ABAQUS 2020, COMOSL-Multiphysics 5.6, and Ansys Maxwell 2018 were used for numerical simulations. |
| Data analysis | Origin 2016 was used to analyse all data, plot the data and calculate the statistical parameters. |

For manuscripts utilizing custom algorithms or software that are central to the research but not yet described in published literature, software must be made available to editors and reviewers. We strongly encourage code deposition in a community repository (e.g. GitHub). See the Nature Portfolio guidelines for submitting code & software for further information.

## Data

Policy information about availability of data

All manuscripts must include a data availability statement. This statement should provide the following information, where applicable:

- Accession codes, unique identifiers, or web links for publicly available datasets
- A description of any restrictions on data availability
- For clinical datasets or third party data, please ensure that the statement adheres to our policy

The main data supporting the results in this study are available within the paper and its Supplementary Information. Source data for Figs. 1–5 is provided with this paper.

## Human research participants

Policy information about studies involving human research participants and Sex and Gender in Research.

| | |
|---|---|
| Reporting on sex and gender | One healthy participant (male) was recruited. |
| Population characteristics | One healthy participant (age 28) was recruited. |
| Recruitment | The healthy participant (age 28; male) were recruited from MU campus through word of mouth. All human subjects gave written and informed consent before participation in the studies. There are no self-selection bias or other bias. |
| Ethics oversight | Institutional Review Board at the University of Missouri-Columbia (number 2010272). |

Note that full information on the approval of the study protocol must also be provided in the manuscript.

# Field-specific reporting

Please select the one below that is the best fit for your research. If you are not sure, read the appropriate sections before making your selection.

☒ Life sciences ☐ Behavioural & social sciences ☐ Ecological, evolutionary & environmental sciences

For a reference copy of the document with all sections, see nature.com/documents/nr-reporting-summary-flat.pdf

# Life sciences study design

All studies must disclose on these points even when the disclosure is negative.

| | |
|---|---|
| Sample size | For the on-body evaluation of chemical sensors, one subject was involved in this study. No statistical methods were used to pre-determine sample sizes but one subject is sufficient to determine whether the device works properly. One healthy subject was recruited because none of the data collected during this study are intended for clinical interpretation. The results can only be used to determine if the device works. |
| Data exclusions | No data were excluded. |
| Replication | All attempts at replication (three times) were successful when following the device-fabrication process described in the paper. |
| Randomization | Since only one subject was involved in this study, randomization was therefore not relevant to the study. |
| Blinding | Blinding was not relevant since only one subject was involved in this study. |

# Reporting for specific materials, systems and methods

We require information from authors about some types of materials, experimental systems and methods used in many studies. Here, indicate whether each material, system or method listed is relevant to your study. If you are not sure if a list item applies to your research, read the appropriate section before selecting a response.

### Materials & experimental systems

| n/a | Involved in the study |
|---|---|
| ☒ | ☐ Antibodies |
| ☒ | ☐ Eukaryotic cell lines |
| ☒ | ☐ Palaeontology and archaeology |
| ☐ | ☒ Animals and other organisms |
| ☒ | ☐ Clinical data |
| ☒ | ☐ Dual use research of concern |

### Methods

| n/a | Involved in the study |
|---|---|
| ☒ | ☐ ChIP-seq |
| ☒ | ☐ Flow cytometry |
| ☒ | ☐ MRI-based neuroimaging |

## Animals and other research organisms

Policy information about studies involving animals; ARRIVE guidelines recommended for reporting animal research, and Sex and Gender in Research

| | |
|---|---|
| Laboratory animals | Adult female Swiss Webster mice (10-14 weeks old) from Charles River Laboratories were used for surgical implantation of the |

| | |
|---|---|
| Laboratory animals | device. |
| Wild animals | No wild animals were used in the study. |
| Reporting on sex | We demonstrated the implantation of stretchable wireless optoelectronic device without recording any sex-related signals, therefore sex is irrelevant in this study . |
| Field-collected samples | No field collected samples were used in the study. |
| Ethics oversight | All animal procedures were performed in accordance with the National Institutes of Health Guide for the Care and Use of Laboratory Animals and approved by the University of Missouri Animal Care and Use Committee. |

Note that full information on the approval of the study protocol must also be provided in the manuscript.